

1 **How size and trigger matter: analyzing rainfall- and earthquake-triggered landslide inventories**  
2 **and their causal relation in the Koshi River basin, Central Himalaya**

3  
4 Jianqiang Zhang<sup>1,2</sup>, Cees J. van Westen<sup>2</sup>, Hakan Tanyas<sup>2</sup>, Olga Mavrouli<sup>2</sup>, Yonggang Ge<sup>1</sup>, Samjwal Bajrachary<sup>3</sup>,  
5 Deo Raj Gurung<sup>3</sup>, Megh Raj Dhital<sup>4</sup>, Narendral Raj Khanal<sup>5</sup>

6 <sup>1</sup>Key Laboratory of Mountain Hazards and Surface Process/Institute of Mountain Hazards and Environment, Chinese Academy of  
7 Sciences, Chengdu, China.

8 <sup>2</sup>Faculty of Geo-Information Science and Earth Observation (ITC), University of Twente, the Netherlands.

9 <sup>3</sup>International Centre for Integrated Mountain Development (ICIMOD), Lalitpur, Nepal.

10 <sup>4</sup>The Department of Geology, Tri-Chandra Multiple Campus, Ghantaghar, Kathmandu, Nepal.

11 <sup>5</sup>Central Department of Geography, Tribhuvan University, Kathmandu, Nepal.

12 *Correspondence to:* Jianqiang Zhang(zhangjq@imde.ac.cn)

13  
14 **Abstract:** Inventories of landslides caused by different triggering mechanisms, such as earthquakes, extreme rainfall  
15 events or anthropogenic activities, may show different characteristics in terms of distribution, contributing factors and  
16 frequency-area relationships. The aim of this research is to study such differences in landslide inventories, and the  
17 effect they have on landslide susceptibility assessment. The study area is the watershed of the trans-boundary Koshi  
18 River in central Himalaya, shared by China, Nepal and India. Detailed landslide inventories were generated based on  
19 visual interpretation of remote sensing images and field investigation for different time periods and triggering  
20 mechanisms. Maps and images from the period 1992 to 2015 were used to map 5,858 rainfall-triggered landslides and  
21 after the 2015 Gorkha earthquake, an additional 14,127 co-seismic landslides were mapped. A set of topographic,  
22 geological and land cover factors were employed to analyze their correlation with different types and sizes of  
23 landslides. The results show that the frequency - area distributions of rainfall- and earthquake-triggered landslides  
24 varied considerably, with the former one having a larger frequency of small landslides. Also topographic factors varied  
25 considerably for the two triggering events, with both altitude and slope angle showing significantly different patterns  
26 for rainfall-triggered and earthquake-triggered landslides. Landslides were classified into two size groups, in  
27 combination with the main triggering mechanism (rainfall- or earthquake-triggered). Susceptibility maps for different  
28 combinations of landslide size and triggering mechanism were generated using logistic regression analysis. The  
29 different triggers and sizes of landslide data were used to validate the models. The results showed that susceptible areas  
30 for small and large size rainfall- and earthquake-triggered landslides differed substantially, while susceptibility maps  
31 for different size of earthquake-triggered landslides were similar.

32  
33 **Key words:** landslides, rainfall-triggered, earthquake-triggered, frequency-area analysis, susceptibility assessment,

34 Nepal

35

36 **1. Introduction**

37 Landslides are one of the most harmful geological hazards causing substantial fatalities and loss of property  
38 worldwide, affecting settlements, agriculture, transportation infrastructure and engineering projects (Dilley et al. 2005;  
39 Petley, 2012; Zhang et al., 2015; Haque et al., 2016). Among the various characteristics that determine the potential  
40 damage of landslides, size plays an important role, as well as velocity, depth, impact pressure, or displacement which  
41 differs for the various mass movement types. Volume may be an even more important landslide characteristic than size,  
42 but this is difficult to measure as it requires specific geophysical or geotechnical methods that can be applied at a site  
43 investigation level, or the use of multi-temporal Digital Elevation Models (SafeLand, 2015; Martha et al., 2017a).  
44 Therefore, empirical relations between landslide area and volume are generally used (Hovius et al, 1997; Dai and Lee,  
45 2001; Guzzetti et al., 2008; Larsen et al., 2011; Klar et al., 2011; Larsen and Montgomery, 2012). To investigate  
46 whether earthquake- and rainfall-triggered landslides inventories have similar area-frequency distributions, area-  
47 volume relations and spatially controlling factors, it is important to collect event-based landslide inventories. The  
48 difficulty is to collect complete inventories that are independent for earthquakes and rainfalls in same study area.

49 The quality of a landslide inventory can be indicated by its accuracy, which refers to the correctness in location and  
50 classification of the landslides, and its completeness, which measures how many of the total number of landslides in  
51 the field were actually mapped (Guzzetti et al., 2012). The accuracy and completeness have a large influence on the  
52 quality and reliability of the susceptibility and hazards maps that are either using the inventory as input (e.g. in  
53 statistical modelling) and in validation (e.g. statistical and physically-based modeling) (Li et al., 2014). There are  
54 several explanations why landslide inventories differ in frequency-area distribution, such as the under sampling of  
55 small slides (Stark and Hovius, 2001), or the amalgamation, the merging of several landslides into single polygons  
56 (Marc and Hovius 2015).

57 Landslides might be triggered by various processes, among which anthropogenic activities, volcanic processes, sudden  
58 temperature changes, earthquakes and extreme rainfall (Highland and Bobrowski, 2008). The latter two are the most  
59 frequently occurring, and causing the highest number of casualties (Keefer, 2002; Petley, 2012; Kirschbaum et al,  
60 2015; Froude and Petley, 2018). Comparing landslide inventories for the same area and for the same triggering event  
61 has been carried out by several authors (e.g. Pellicani and Spilotro, 2015; Tanyas et al., 2017a). Some studies took  
62 independent earthquake- and rainfall-triggered landslide inventories to compare the characteristics of landslides  
63 induced by different triggers. Malamud et al.(2004) compared earthquake-triggered landslides from the Northridge  
64 earthquake, Umbria snowmelt-triggered landslide and Guatemala rainfall-triggered landslide as examples, and  
65 concluded that the three frequency-area distributions were in good agreement with each other. Meunier et al. (2008)

66 compared earthquake-triggered landslides, from Northridge, Chi-Chi Finisterre Mountains (Papua New Guinea), to  
67 evaluate topographic site effects on the distribution of landslides. Tanyas et al. (2017b) created a database with 363  
68 landslide-triggering earthquakes and 64 digital landslide inventories, which were compared. The number of studies  
69 that compare earthquake-triggered landslide with rainfall triggered ones for the same area is less numerous. They are  
70 mostly focusing on mapping rainfall-induced landslides after an earthquake, such as for the 1999 Chi-Chi earthquake  
71 (Lin et al., 2006; 2008), the 2005 Kashmir earthquake (Saba et al., 2010) or the 2008 Wenchuan earthquake (Tang et al.  
72 2010; Marc et al., 2015; Tang et al., 2016; Fan et al., 2018a).

73 The problem with the studies indicated above is that rainfall-triggered landslides that occur shortly after a major  
74 earthquake are generally following the same spatial patterns, due to the availability of large volumes of landslide  
75 materials of the co-seismic landslides (Hovius et al., 2011; Marc et al., 2015; Tang et al., 2016; Fan et al., 2018a), so  
76 for the post-earthquake landslide susceptibility assessment, the location of the co-seismic landslides is a crucial factor.  
77 There are very few studies that have validated landslide susceptibility maps with independent landslide inventories of  
78 triggering events that occurred after the maps were produced. Chang et al. (2007) used landslides triggered by a major  
79 earthquake and a typhoon prior to the earthquake to develop an earthquake-induced model and a typhoon-induced  
80 model. The models were then validated by using landslides triggered by three typhoons after the earthquake.  
81 According to the results, typhoon-triggered landslides tended to be near stream channels and earthquake-triggered  
82 landslides were more likely to be near ridge lines. Although landslide size is often considered important in hazard and  
83 risk assessment, it is generally not considered as a separate component of the susceptibility assessment. The different  
84 relation with contributing factors of earthquake-triggered and rainfall-triggered landslides may also be related to the  
85 size distribution (Korup et al. 2007). For instance, Fan et al. (2012) concluded that small ( $<10 \times 10^4 \text{m}^3$ ) rainfall-  
86 triggered landslide and earthquake-triggered landslides have similar runout distances, whereas for larger landslides  
87 earthquake-triggered ones showed longer runouts. Peng et al. (2014) analyzed the landslides in the Three Gorges area  
88 and found that different landslide sizes had different relations with contributing factors.

89 The aim of this study is to investigate the differences in the characteristics of earthquake-triggered and rainfall  
90 triggered landslides in terms of their frequency-area relationships, spatial distributions and relation with contributing  
91 factors, and to evaluate whether separate susceptibility maps generated for specific landslide sizes and triggering  
92 mechanism are better than a generic landslide susceptibility assessment including all landslide sizes and triggers. This  
93 research aims to address a number of questions related to the difference of using earthquake-induced and rainfall-  
94 induced landslide inventories for the generation of landslide susceptibility maps. The first question is whether different  
95 landslide size groups are controlled by different sets of contributing factors. The second question that will be addressed  
96 is whether it is possible to utilize inventories of earthquake-triggered landslides (ETL) as inputs for analyzing the  
97 susceptibility of rainfall-triggered landslides (RTL) and vice versa.

批注 [h1]: Reference paper was added below

98

## 99 **2. Study area**

100 The study was carried out in the Koshi River basin, which is a trans-boundary basin located in China, Nepal and India  
101 in the central Himalayas (Fig. 1a). The mountainous regions in the upper reaches of the basin where landslides have  
102 occurred are located in China and Nepal, and the Indian part consists of relatively flat areas. The elevation of Koshi  
103 River basin varies from 60 m a.s.l. at the outlet in India up to 8,844 m at the highest point at Mount Everest. The  
104 Koshi basin can be classified into 6 physiographic zones from South to North: Terai, Siwalik Hills, Mahabharat Lekh,  
105 Middle Mountains, High Himalaya, and Tibetan Plateau (Gurung and Khanal 1987; Dhital 2015). Considering the  
106 distribution of landslides, the Tibetan plateau in the upper reaches and the plains in the lower reaches were excluded.

107 In the Koshi Basin, the major geological structures have an approximate east–west orientation, such as the foreland  
108 thrust-fold belt, Main Central Thrust (MCT), South Tibetan Detachment System (STDS) and the Yarlung Zangbo  
109 Suture Zone (YZSZ) (Gansser, 1964; Dhital, 2015). The southernmost part of the basin consists of the Quaternary  
110 sediments underlain by the Neogene Siwaliks. The Siwaliks comprise soft mudstones, sandstones and conglomerates.

111 In this part of the foreland basin, a number of emergent and blind imbricate faults originate from the Main Himalayan  
112 Thrust. The overlying Lesser Himalayan succession forms duplexes and imbricate stacks. The Proterozoic to Miocene  
113 rocks of the Lesser Himalaya include limestones, dolomites, slates, phyllites, schists, quartzites, and gneisses (Dhital,  
114 2015). A regional-scale thrust MCT separates the Lesser Himalayan sequence from the overlying Higher Himalayan  
115 crystallines, which consist of medium- to high-grade metamorphic rocks (e.g., schists, quartzites, amphibolites,  
116 marbles, gneisses, and migmatites) and granites aged from the Proterozoic to Miocene. The STDS delineates the  
117 Higher Himalayan rocks from the overlying Tethyan sedimentary sequence of Paleozoic–Cenozoic age (Gansser, 1964;  
118 Burg et al., 1984; Hodges et al., 1996) (Fig. 1b).

119 In the study area there are three main tributaries of the Koshi River: the Arun (main branch) coming from the north, the  
120 Sun Koshi from the west and Tamor from the east. Nearly every year, during the monsoon period, which generally  
121 lasts from June to September, the area is affected by rainfall-triggered landslides. Dahal and Hasegawa (2008) used a  
122 dataset of 193 landslides occurring from 1951 to 2006, part of which were from the Koshi River basin, to generate a  
123 threshold relationship between rainfall intensity, rainfall duration, and landslide initiation.

124 The area was severely affected by the Gorkha earthquake, with a moment magnitude of 7.8 on 25 April 2015. The  
125 epicenter was located near Gorkha, which is about 80km west of the study area. A second major earthquake occurred  
126 along the same fault on 12 May 2015 with a moment magnitude of 7.3 with the epicenter located inside the Koshi  
127 River basin. The second event is considered as a major aftershock of the main Gorkha earthquake. Both events  
128 triggered many landslides (Collins and Jobson 2015; Kargel et al. 2016; Zhang et al. 2016; Martha et al. 2017b).

129

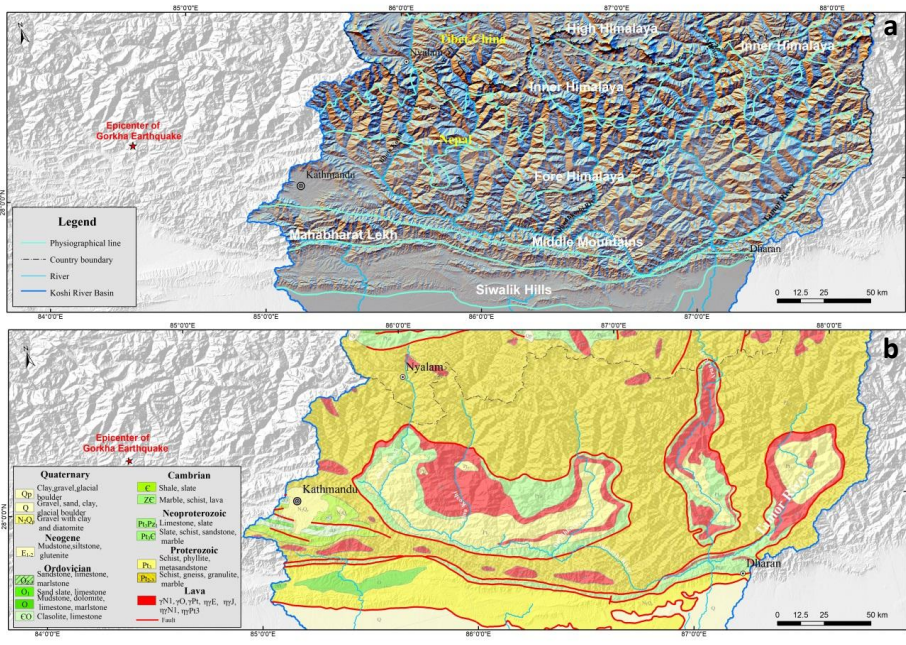


**Fig. 1** Maps showing the study area (a) Physiographic zones of the Koshi River basin; (b) Geological map showing the main geological zones (Dhital, 2015; Zhang et al., 2016).

**3. Input data**

The study requires a series of landslide inventory maps, and contributing factor maps, which were generated for the middle part of the Koshi basin, where most of the landslides were concentrated. Two landslide inventories were generated: a pre-2015 inventory showing rainfall-triggered landslides, and a co-seismic landslide map for the 2015 Gorkha earthquake. The pre-2015 inventory map was generated using topographic maps, multi-temporal Google Earth Pro images and Landsat ETM/TM images. We were able to digitize landslide polygons from the available 1:50,000 scale topographic maps, which cover only the Nepalese part of the Koshi River basin. These maps were generated from aerial photographs acquired in 1992, and active landslides with a minimum size of 450 m<sup>2</sup> visible on these images were marked as separate units. The landslides could not be separated in initiation and accumulation zones, and also no classification of landslide types could be done, as this was not indicated on the topographic maps. A set of pre-2015 Landsat ETM/TM images were available for the entire study area, from which the post 1992 and pre-2015 landslides. Pre-2015 landslides were also mapped from historical images using Google Earth Pro Historical Imagery

146 Viewer which contains images from 1984 onwards. Although the oldest images are Landsat images, the more recent  
147 ones have much higher resolution, although not covering the whole study area in equal level of detail. By comparing  
148 the different images for the period between 1992 and 2015 we were able to recognize most of the landslides. We  
149 carried out field verification for a number of samples. Images from Google Earth were downloaded and geo-  
150 referenced and landslides were mapped using visual image interpretation and screen digitizing. A total of 5,858 rainfall  
151 induced landslides were identified in the Koshi River basin.

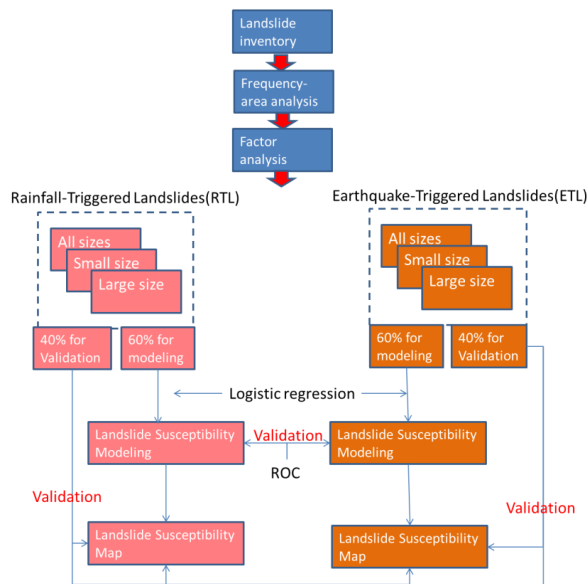
152 After the 2015 April 25<sup>th</sup> Gorkha earthquake, a substantially complete earthquake-triggered landslide inventory was  
153 created by Roback et al. (2017). They mapped landslides using high-resolution (<1m pixel resolution) pre- and post-  
154 event satellite imagery. In total 24,915 landslide areas were mapped, of which 14,022 landslides were located in the  
155 Koshi river basin. Chinese GaoFen-1 and GaoFen-2 satellites imageries (with 2.5m resolution) of the CNSA (China  
156 National Space Administration), which are part of the HDEOS (High-Definition Earth Observation Satellite) program,  
157 were employed to validate this landslide inventory. These images were captured during 27 April, 2015 to May 14  
158 2015. Finally 15 landslide polygons were deleted, and 120 landslides were added to the inventory.

159 For the susceptibility assessment, we extracted the point located in the highest part of the landslides, as indicative of  
160 the initiation conditions. Different DEMs, such as ASTER GDEM, SRTM Digital Elevation Model with both 90 m and  
161 30m spatial resolution, as well as ALOS PALSAR DEM were evaluated to use in this study. After careful analysis  
162 however, both ASTER GDEM and 30m SRTM contained many erroneous data points, ALOS PALSAR DEM with  
163 highest resolution of 12.5m, was utilized in this study. ESRI ArcGIS software enabled the calculation of topographical  
164 factors including slope gradient, aspect, and curvature. Streams and gullies were obtained through DEM processing,  
165 and the drainage density was calculated. The land cover dataset GlobeLand30 with 30×30m spatial resolution,  
166 developed by the National Geomatics Center of China, was employed in this study. The land cover types include  
167 cultivated land, forest, grassland, shrub land, wetland, water bodies, tundra, artificial surfaces and bare land.  
168 Geological maps of Nepal, and Tibet were obtained from Chengdu Geological Survey Center of the China Geological  
169 Survey. The Peak Ground Acceleration data for the Gorkha earthquake were obtained from USGS Shakemap, which  
170 was designed as a rapid response tool to portray the extent and variation of ground shaking throughout the affected  
171 region immediately following significant earthquakes (Wald et al., 1999). Given the rather low resolution of the input  
172 data, the relation with landslides as small as 50m<sup>2</sup> may not be optimal, especially also considering the rather long time  
173 period over which land cover changes have occurred in many areas. But given the regional scale of this analysis, the  
174 use of higher resolution data was unfortunately not a viable option.

#### 175 4. Methods

176 Figure 2 gives an overview of the method followed in this study. The landslide inventories were subdivided into  
177 training and test datasets. It is a generally accepted method in literature to separate the landslide dataset into a training

178 and validation set (e.g. Hussin et al. 2016; Reichenbach et al., 2018), although the separation thresholds differs among  
 179 authors. We decided to select 60% of the landslide data as training data for the modeling, and 40% for the validation.  
 180 We examined the frequency-area distribution of the gathered inventories using the method described by Clauset et al.  
 181 (2009). They proposed a numerical method to identify the slope of power-law distribution ( $\beta$ ) and the point where  
 182 frequency-area distribution diverges from the power-law (cutoff point).  
 183 Based on the frequency area distribution the RTL and ETL inventories were separated in two size-groups each. Initially  
 184 bivariate statistical analysis was used for the different types and sizes of landslides, to investigate the correlation  
 185 between landslides with contributing factors. After selecting the relevant factors, the logistic regression method was  
 186 used to build the susceptibility model for each size group. The Logistic Regression method is the most commonly used  
 187 model in landslide susceptibility assessment (Ayalew and Yamagish 2005; Bai et al. 2010; Das et al. 2000; Nandi and  
 188 Shakoor 2010; Wang et al. 2013). For the susceptibility modeling of RTL, the following factors were used: altitude  
 189 ( $x_1$ ), slope gradient ( $x_2$ ), curvature ( $x_3$ ), slope aspect ( $x_4$ ), relative relief ( $x_5$ ), drainage density ( $x_6$ ), lithology ( $x_7$ ),  
 190 distance to faults ( $x_8$ ), land cover type ( $x_9$ ), precipitation during monsoon( $x_{10}$ ). For the susceptibility modeling of ETL,  
 191 precipitation during monsoon( $x_{10}$ ) was instead of peak ground acceleration ( $x_{10}$ ). The statistical software R developed  
 192 at Bell Laboratories was used to build the models for different types and sizes of landslide respectively. ROC (Receiver  
 193 Operating Characteristic) curves (Fawcett, 2006) were used to verify the accuracy of the susceptibility models, and  
 194 finally six landslide susceptibility maps were generated and compared (Fig. 2).



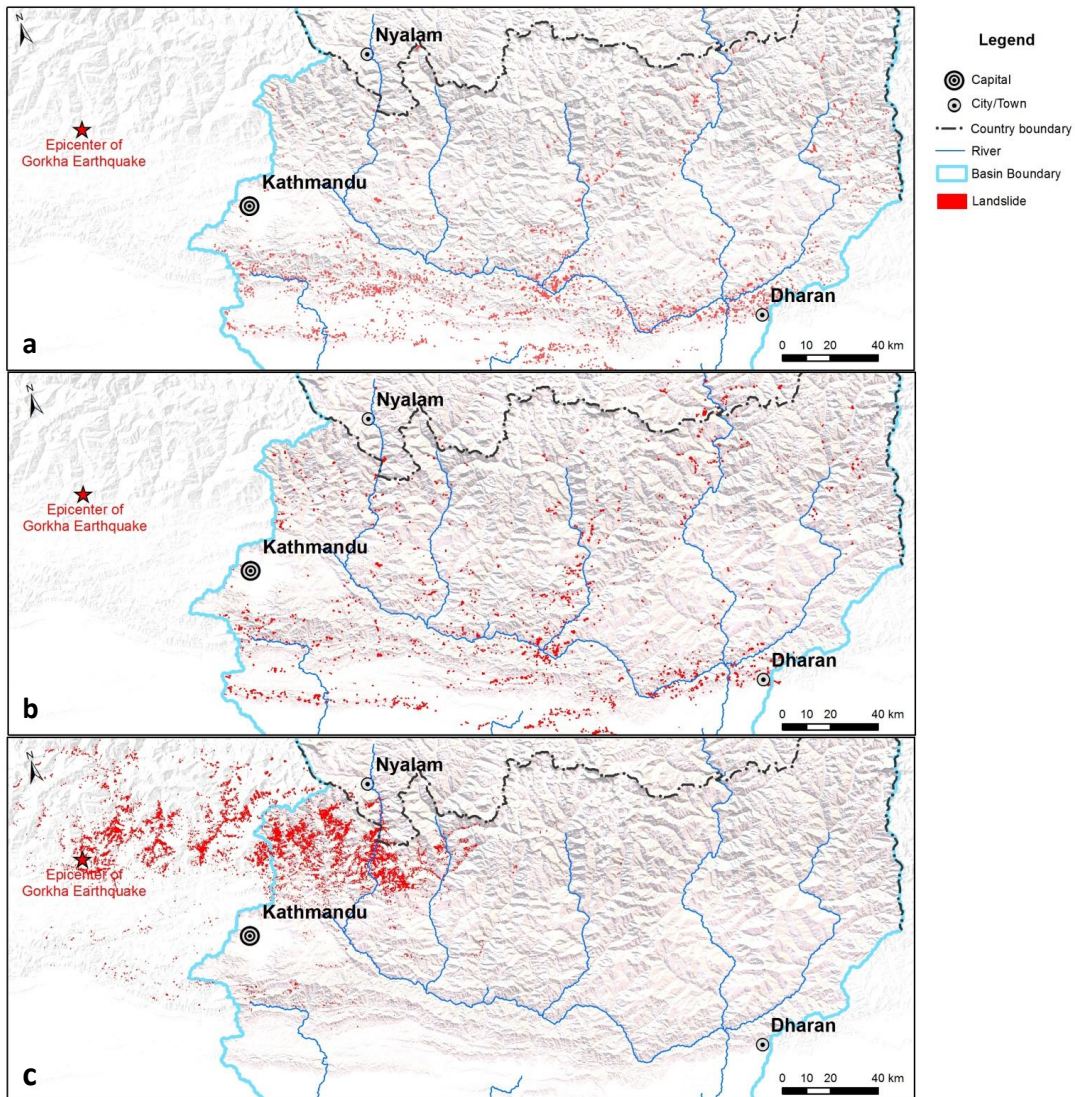
196 **Fig. 2** Methodology for susceptibility assessment to different types and sizes of landslide

197

198 **5. Landslide characteristics**

199 In the Koshi River basin, a total of 5,858 RTL were mapped. The Gorkha earthquake triggered more than 25,020  
200 landslides, of which 14,127 were located in the Koshi River basin. Landslide characteristics were analyzed based on  
201 frequency-area distribution and factor statistics (Fig. 3).

批注 [h2]: Base on the new inventory, numbers of ETL were updated



202 **Fig. 3** Landslide inventories of the Koshi River basin (a) Rainfall induced landslide inventory of events before 1992; (b)  
 203 Rainfall induced landslide inventory for the period between 1992 to 2015; (c) Inventory of landslides triggered by the  
 204 2015 Gorkha earthquake (Roback et al. 2017).  
 205

批注 [h3]: Fig.3c was changed base on Roback's landslide inventory

## 206 5.1 Landslide frequency-area distributions

207 Size statistics of landslides are analyzed using frequency-area distribution curves of landslides (e.g., Malamud et al.,  
208 2004). There is a large literature arguing that frequency-area distribution of medium and large landslides has power-  
209 law distribution, which diverges from power-law towards smaller sizes (e.g., Hovius et al., 1997; 2000; Malamud et  
210 al., 2004). Given this argument, we can identify the divergence point of frequency-area distribution curve to determine  
211 a site specific threshold values referring to the limit between medium and small landslides.

212 The frequency-area distributions (FAD) of landslides were separately analyzed for both RTL and ETL inventories (Fig.  
213 4). For the RTL both landslide inventory datasets of before 1992 and 1992~2015 were analyzed (Fig. 4a). For the ETL  
214 of the Gorkha earthquake, landslides located in the Koshi River basin were analyzed separately from the entire  
215 landslide-affected area. We obtained similar  $\beta$  values for the RTL triggered before 1992 ( $\beta = 2.44$ ) and triggered from  
216 1992 to 2015 ( $\beta = 2.38$ ) (Fig. 4a). On the other hand, we observe larger differences between the  $\beta$  values obtained for  
217 ETL inventories created for both Koshi River basin and entire landslide-affected area (Fig. 4b).

218 We also examine the cutoff values of inventories. The historical RTL inventories and ETL inventory that we examined  
219 for both Koshi River basin and entire landslide-affected area gave similar cutoff values changing from 24,884 m<sup>2</sup> to  
220 32,913 m<sup>2</sup> (Fig. 4). This finding shows that, the limit between small and large landslides are consistently obtained from  
221 these inventories about 30,000 m<sup>2</sup>. Given this finding, the proposed landslide size classification system of China the  
222 Tong et al. (2013) seems like an acceptable approach for our study area. They proposed a classification with landslides  
223 with an area smaller than 10,000 m<sup>2</sup> as small, those with an area between 10,000 m<sup>2</sup> and 100,000 m<sup>2</sup> as medium, and  
224 those with larger sizes than 100,000 m<sup>2</sup> as large size landslide. Considering this study, and the cutoff values calculated  
225 in our study, 30,000 m<sup>2</sup> was picked as a threshold value for large landslides.

226

227

228

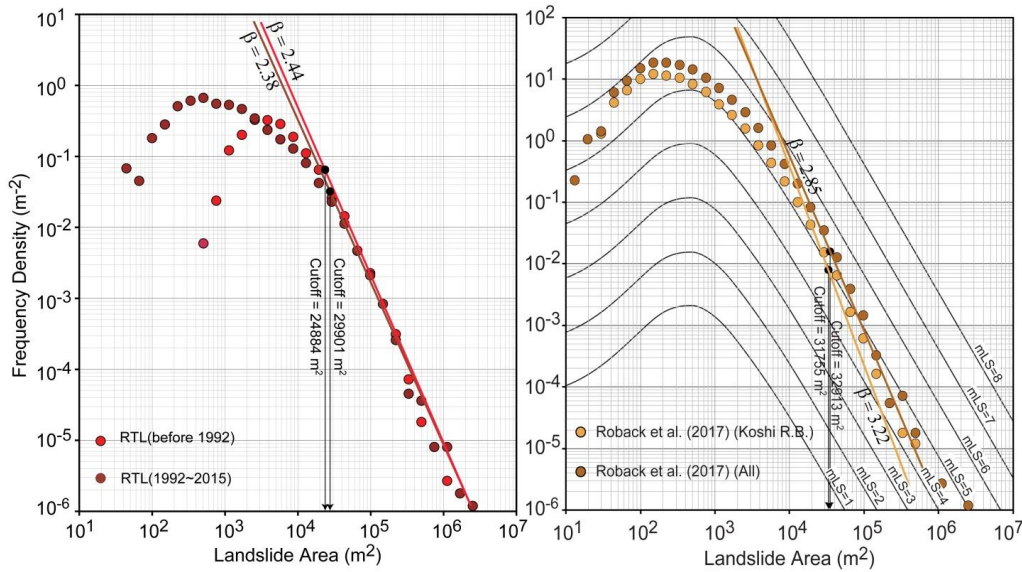


**Fig. 4** Landslide frequency - area distributions of (a) RTL inventories, (b) ETL inventories created for Koshi River basin and (c) ETL inventories created for the entire landslide-affected area of the 2015 Gorkha, Nepal earthquake (Roback's landslide inventory was validated). Cutoff and  $\beta$  values are calculated using the method proposed by Clauset et al. (2009).

批注 [h4]: Fig.4b the curves was redrawn base on validated landslide inventory of Roback's(2017)

Based on the results of the FAD analysis, that resulted in similar cutoff values for the RTL and ETL and similar  $\beta$  values, we subdivided them into two size-groups, with 30,000 m<sup>2</sup> as threshold value (Table 1). The results will therefore be more reliable for the class above the threshold of 30,000 m<sup>2</sup>, where under sampling is not an issue, then for the small landslide class, which has different rollover points, and completeness levels.

**Table 1** Numbers for different types and sizes of landslide in Koshi River basin

	Rainfall-triggered landslides (RTL)			Earthquake-triggered landslides (ETL)		
	All sizes	Small size	Large size	All sizes	Small size	Large size
Total	5,858	5267	591	14,127	13981	146
Modelling	3,515	3160	355	8476	8388	88
Validation	2,343	2107	236	5650	5593	58

批注 [h5]: Due to the change of threshold, the numbers of large size and small size of landslide also changed.

241

242 5.2 Correlation of landslides with contributing factors

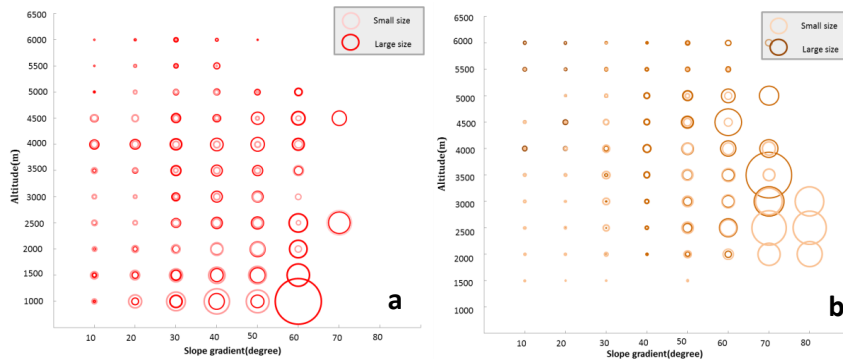
243 In order to evaluate their relation with landslide occurrence the factor maps were analyzed using the Frequency Ratio  
244 method (Razavizadeh et al. 2017).

$$FR = \frac{E/F}{M/L}$$

245 where *E* is the area of landslides in the conditioning factor group, *F* is the area of landslides in the entire study area, *M*  
246 is the area of the conditioning factor group, and *L* is the entire study area. The analysis was carried out for different  
247 triggers and size groups, and each time two factors were combined (e.g. altitude with slope gradient, altitude with slope  
248 direction, lithology with slope gradient). The results are summarized in Fig. 5. Fig. 5a&b show that rainfall triggered  
249 landslides (RTL) are more frequent in low altitude areas than earthquake triggered landslides (ETL). However, it is  
250 important to keep in mind that the ETL is an event inventory of a single earthquake, where the epicenter was located at  
251 higher altitude (See Fig. 3) and the RTL is a multi-temporal inventory, showing the accumulated inventory of many  
252 individual events.

253 Fig. 5 c&d show the relation with slope and lithology. RTL are concentrated on Proterozoic metamorphic lithological  
254 units (Pt3), consisting of schist, phyllite and metasandstone, and in Quaternary molasse ( N2Qp ) units, consisting of  
255 gravel and clay (See Fig. 1). ETLs are linked to units consisting of shale and slate (Pt3e), and Cambrian units  
256 consisting of shale and slate (e) and marble, schist and lava (Ze).

257



批注 [h6]: A new method, Frequency Ratio, was brought into this part, to analyze correlation of landslide with double contributing factors.

258

259

260

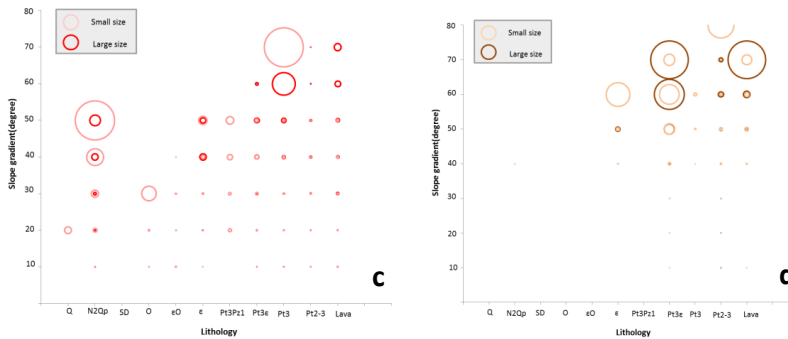


**Fig. 5** Correlation between landslides and other factors for rainfall triggered landslides (RTL) on the left side, and earthquake-triggered landslides (ETL) on the right side. The size of the circles indicate the value of the Frequency Ratio. a & b: Relation between altitude and slope gradient; c & d: Relation between Lithology and slope gradient.

批注 [h7]: This figure was redrawn base on FR method.

## 6. Landslide susceptibility assessment

### 6.1 Landslide susceptibility models

The following factors were used for the susceptibility modeling of RTL: altitude( $x_1$ ), slope gradient( $x_2$ ), curvature( $x_3$ ), slope aspect( $x_4$ ), relative relief( $x_5$ ), drainage density( $x_6$ ), lithology( $x_7$ ), distance to fault( $x_8$ ), land cover type( $x_9$ ) and precipitation during monsoon( $x_{10}$ ). Peak Ground Acceleration (PGA) was used instead of precipitation for the susceptibility modeling of ETL (Fig. 6). The R software was used to build the models by Logistic Regression method for different types and sizes of landslide respectively (Table 2). ROC curves were generated to verify the accuracy of each susceptibility model, and value of the Area Under Curve (AUC) was calculated (Table 2).

The coefficients for the contributing and triggering factors in the landslide susceptibility models show differences between triggers and different sizes of landslides. Curvature, altitude and slope gradient have a high impact on the susceptibility of RTL, while curvature, PGA, relative relief, and slope gradient have high impact on susceptibility of ETL. The size classes of RTL show larger differences in weight of curvature, relative relief and altitude. For ETL the difference between size classes are largest for factors of PGA, curvature, and relative relief.

批注 [h8]: Precipitation factor was added in the model

281

282

283

284

285

286

287

288

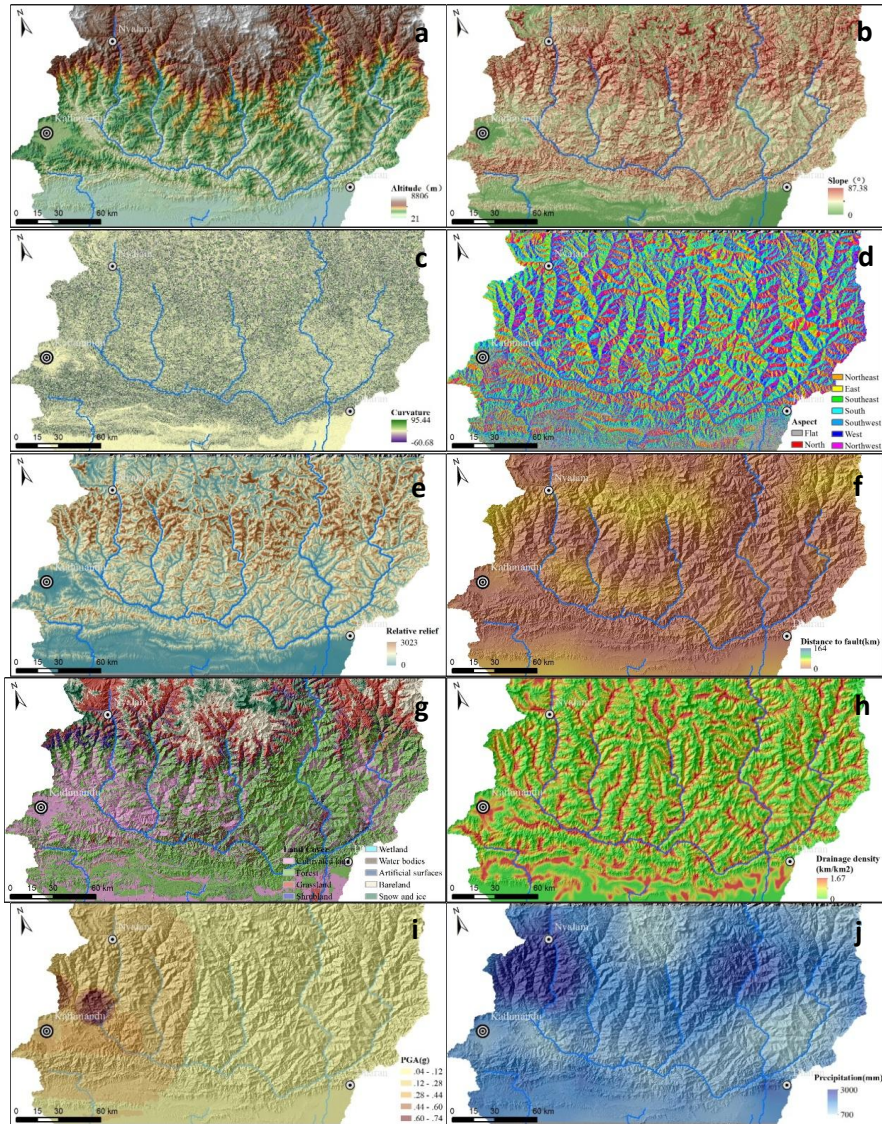


**Fig. 6** Landslide susceptibility assessing factors; a: altitude(Data source: JAXA/METI ALOS PALSAR DEM); b: slope gradient; c: slope curvature; d: slope direction; e: relative relief; f: distance to fault; g: land cover; h: drainage density; i: Peak Ground Acceleration of the 2015 Gorkha earthquake (Peak Ground Acceleration data for the Gorkha earthquake

289 were obtained from USGS Shakemap, which was designed as a rapid response tool to portray the extent and variation  
 290 of ground shaking throughout the affected region immediately following significant earthquakes); j: Average total  
 291 monsoon precipitation (ICIMOD and the National Meteorological information Center of China. This data is the  
 292 average precipitation for the period 1991-2010, for the monsoon season from June to October).

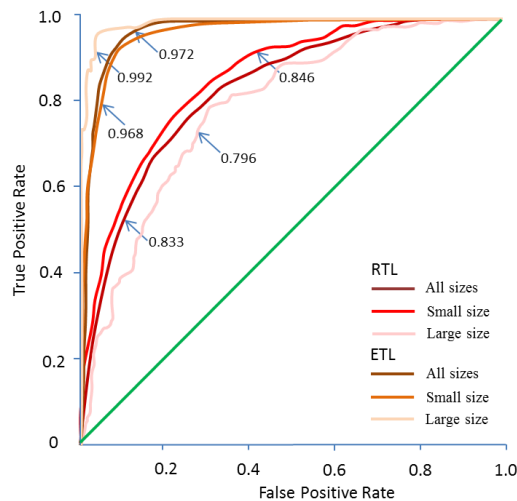
294 **Table 2** Susceptibility models for different triggers and landslide size classes in the Koshi River basin

Landslide type	x <sub>1</sub>	x <sub>2</sub>	x <sub>3</sub>	x <sub>4</sub>	x <sub>5</sub>	x <sub>6</sub>	x <sub>7</sub>	x <sub>8</sub>	x <sub>9</sub>	x <sub>10</sub>	p
All RTL	-6.4317	6.4955	-12.2440	-0.1717	-3.7048	-1.3431	1.0590	-0.7090	1.3725	0.7206	4.3961
Small size RTL	-8.36420	6.33158	-1.37934	-0.09899	-2.68158	-1.91514	1.10489	-0.93464	1.10003	0.98897	-0.54775
Large size RTL	-4.93126	6.47043	7.03034	-0.30706	4.79661	-0.13525	1.49649	-0.49201	1.31034	0.07492	-6.69787
All ETL	-3.3342	5.8510	-8.6844	-0.5513	8.8514	6.3296	3.2108	-0.2472	1.3740	17.4360	-6.4566
Small size ETL	-7.4433	5.8410	-7.5233	-0.1974	5.9871	4.2647	2.6977	1.7495	1.2858	7.5676	-3.3845
Large size ETL	6.939	10.116	-26.355	3.660	16.503	11.678	3.962	-4.039	2.633	28.199	-11.445

批注 [h9]: This new figure was added here, to show all the assessing factor for landslide susceptibility, with data source described.

批注 [h10]: Due to the change of threshold for small size and large size of landslide, the ETL inventory, as well as precipitation factor added for RTL, all the susceptibility models were calculated again.

295  
 296 ROC curves were drawn to verify the accuracy of each susceptibility model (Fig. 7), and the Area Under Curve (AUC)  
 297 was calculated. The AUC values of the ETL models were higher than for RTL, since the ETL were more concentrated  
 298 than the RTL, as the inventory is from one single triggering event, whereas the RTLs are from many different rainfall  
 299 events over a longer time period.



300 **Fig. 7** ROC curves for the susceptibility assessing models to different sizes of RTL and ETL

批注 [h11]: The ROC curves were drawn for the new susceptibility models.

302

## 303 6.2 Results

304 The logistic regression models were employed to the Koshi River basin and in total six susceptibility maps were  
305 generated (Fig. 8). Susceptibility values were classified into four levels: low, moderate, high and very high, based on  
306 the following susceptibility threshold values: 0-0.25, 0.25-0.5, 0.5-0.75 and 0.75-1.

307 The RTL susceptibility map (Fig. 8a) shows that high and very high susceptible are located mostly in the Siwaliks and  
308 in the Mahabharat Lekh region in west-eastern direction and the Middle to High Himalaya region in north-south  
309 direction. The Siwaliks and Mahabharat Lekh regions (Fig 1) have high and very high susceptibility levels for small  
310 landslides, and lower susceptibility levels for large ones. The Middle and High Himalaya region (Fig. 1) has a reverse  
311 situation: high and very high susceptibility levels for large landslides, and lower levels for small ones.

312 The ETL susceptibility map reflects the co-seismic landslide pattern of the Gorkha earthquake, with very high and high  
313 susceptibility in the western part of the Koshi River basin. It is important to note that the ETL susceptibility map only  
314 reflects the characteristics of the Gorkha earthquake and is therefore not a reliable map for future earthquakes that may  
315 have another epicentral location, length of fault ruptures and magnitudes.

316 Both ETL and RTL susceptibility maps show different patterns for the large size landslide class (Fig. 8 c and f),  
317 whereas the maps for small size (Fig 8 b and e) resemble those of all size classes (Fig 8 a and d). This is due to the  
318 relative small fraction of the large size landslides in comparison with the small ones, and their more restricted location,  
319 which gives different weight values for some factor maps (Table 2).

320 The highest susceptibility zones for small size and large size RTL show a large overlapping area, although the area of  
321 these classes is much smaller for large size RTL. In the Siwaliks and Mahabharat Lekh regions high and very high  
322 susceptibility zones for large size RTL are located in the upper steep hillslopes. In the Middle and High Himalaya  
323 region, the highest susceptibility zones for both small size and large size RTL are mostly located on steep slopes along  
324 rivers. The highest susceptibility zones for both small and large size ETL are located in the northwestern part of the  
325 Khoshi basin. For large size ETL these are concentrated in a smaller area to the northeast of Kathmandu (with altitude  
326 higher than 3000m) where small ETL also show high susceptibility in the southeast of Kathmandu.

327

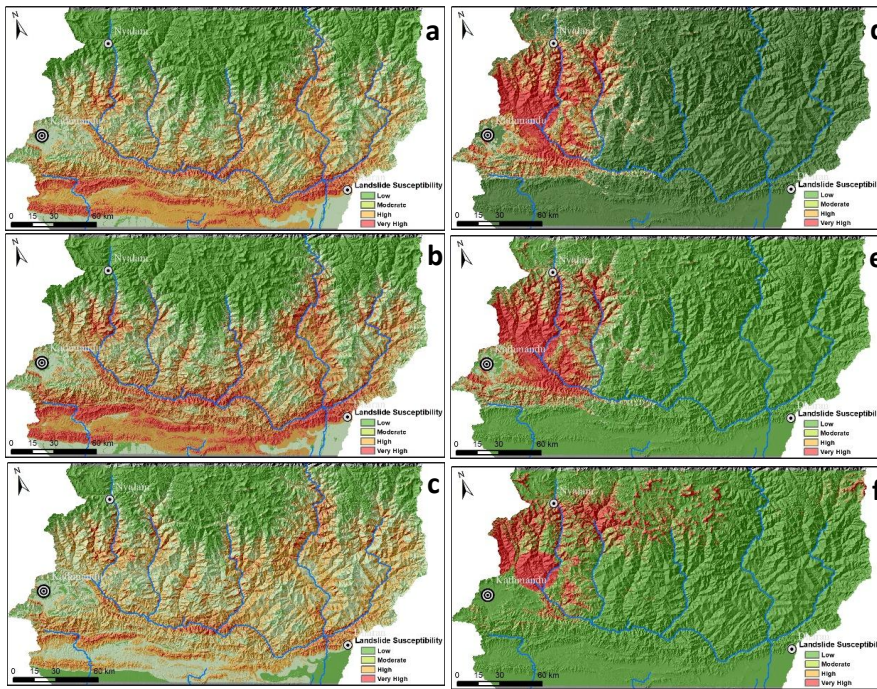


**Fig. 8** Susceptibility maps for different sizes of RTL and ETL: (a) for all RTLs; (b) for small RTLs; (c) for large RTLs; (d) for all ETLs; (e) for small ETLs; (f) for large ETLs.

批注 [h12]: All the susceptibility maps were redrawn according to the new models.

The areal coverage of the landslide susceptibility classes was calculated for each susceptibility map (Fig. 9). Compared to RTL, the ETL susceptibility maps have a larger area with low susceptibility, due to fact that the Koshi River basin is far from the epicenter of Gorkha earthquake, thus the earthquake affected region is only part of the basin. The very high and high susceptible region for ETL is mostly concentrated in the western and southwestern parts of the basin, clearly reflecting the PGA pattern (Fig 6i). The RTL susceptibility also reflects the triggering factor (monsoonal rainfall), with the highest susceptibility in the south of the basin. However, the higher rainfall peak in the Middle and High Himalaya region is less pronounced in the susceptibility maps, as well as in the inventory maps (Fig 3). The higher susceptibility classes for large ETL occupy more area than for small ETL, while the opposite can be observed for RTL.

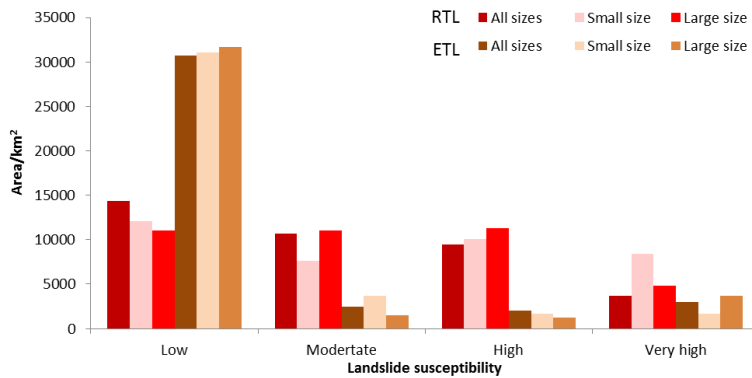
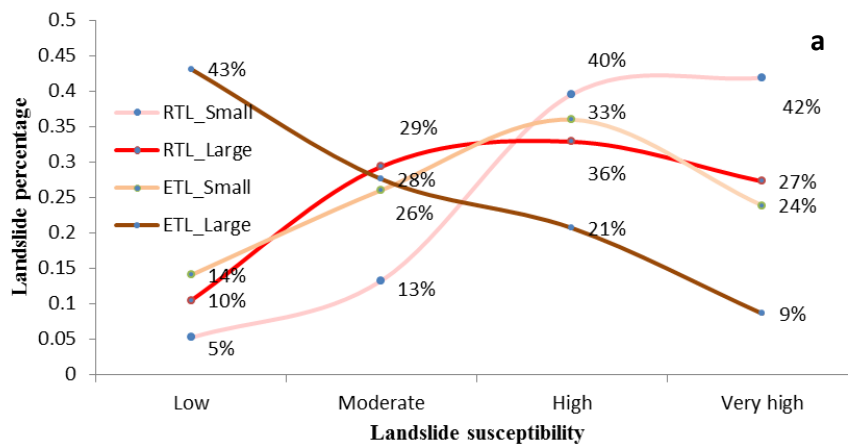


Fig. 9 Coverage of different landslide susceptibility classes for ETL and RTL maps

批注 [h13]: This figure was redrawn base on the new susceptibility maps.

### 7. Validation of landslide susceptibility maps

Different groups of landslide data were used to validate the landslide susceptibility maps for RTL and ETL. For each trigger and size class, the number of landslides was calculated, inside the areas with a certain susceptibility level, to cross-validate the results.



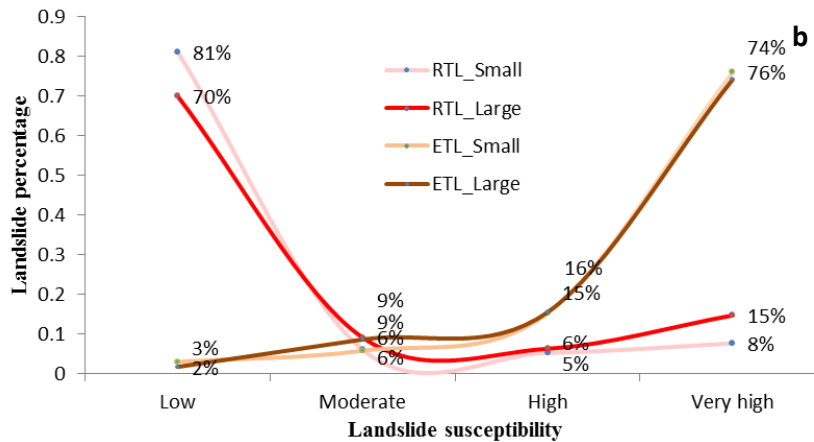


**Fig. 10** Cross validation of the landslide susceptibility maps. (a) The percentage of landslides in the various classes of the RTL susceptibility map. (b) The percentage of landslides in the various classes of the ETL susceptibility map.

批注 [h14]: This figure was redrawn

The percentages of different size RTLs and ETLs in each susceptibility are shown in Fig.10. For the RTL susceptibility map, percentages of of small size and large size landslides show a similar tendency, for both triggers. Most of the landslides were located in high and very high susceptibility zones. Only large size of ETL shows an opposite tendency. There is a marked difference between the percentages of ETL and RTL in the ETL landslide susceptibility classes. the RTL and ETL percentages show completely different patterns. Most of the RTLs (both small and large) are located in the low ETL susceptible regions. Conversely, a large fraction of small size and large size of ETLs are located in the high susceptible regions.

## 8. Discussion and conclusions

This study aimed to analyze independent rainfall- (RTL) and earthquake-triggered landslide (ETL) inventories for a large mountainous watershed in the Himalayas, located in India, Nepal and China. It is important to mention, that the two rainfall-triggered landslide inventories are not event-based inventories (Guzzetti et al., 2012). A major limitation in this work was that we were not able to use separate event-based inventories for RTLs, and only one event-based inventory for ETL. The collection of event-based inventories, both for rainfall and earthquake triggers, remains one of the main challenges in order to advance the study of landslide hazard at a watershed scale.

The two RTL inventories differ in the sense that the 1992 inventory is based on landslides that were large enough to be mapped on the topographic map, where as the inventory between 1992 and 2015 represents the landslides that could be

372 mapped from multi-temporal images over a number of years. Both inventories were lacking a separation into initiation  
373 and accumulation parts, and no separation in landslide types could be made. The effects of amalgamation of landslides  
374 might certainly have played a role in the Frequency Area Distribution (Marc and Hovius, 2015) although we are not  
375 able to quantify this, due to lack of an independent dataset. For the 1992-2015 dataset we were able to control this as  
376 we carried out the image interpretation ourselves, but the pre-1992 inventory could not be verified as the aerial  
377 photographs that were used to generate the updated topographic maps, were not available to us. Although the two  
378 inventories differ substantially with respect to the number of small landslides, it is striking to see that the cut-off  
379 values, and  $\beta$  values in the Frequency Area Distribution (FAD) are similar. It is very difficult to obtain a complete  
380 event-based landslide inventory for rainfall induced landslides in Nepal, as landslides are generally generated by a  
381 number of extreme rainfall events during the monsoon, which can not be separated, as the area is cloud-covered  
382 through most of the period. The earthquake triggered landslide distribution is an event-based inventory, for a single  
383 earthquake (2015 Gorkha) and based on an extensive mapping effort by Roback et al. (2017) resulting in an inventory  
384 that can be considered as complete (Tanyas et al., 2017a). When comparing the FAD for RTL and ETL it is striking  
385 that the size-frequency distributions for both ETL and RTL show very similar behaviour for landslides above the cut-  
386 off value of 30,000 m<sup>2</sup>. Although there is no concensus regarding the factors dictating the power-law distribution of  
387 landslides, there is an accumulating evidence that topography has to be one of an important controlling factors (e.g.,  
388 Liucci et al., 2017; Frattini and Crosta, 2013; ten Brink et al., 2009). Our finding regarding similar cutoff values  
389 obtained from different inventories created for the same area is also supporting this argument.

390 The pattern of the triggers (precipitation in the Monsoon for RTL, and PGA distribution for ETL) have major influence  
391 on the distribution of landslides and susceptibility zones. These trigger patterns differ substantially. When moist  
392 airflow from the India Ocean crosses over the Mahabharat Lekh, the intensity of precipitation reduces because the  
393 altitude lowers and temperature rises. As the airflow continues northwards to the Middle Mountains and Transition  
394 Belt, it rises again and consequently induces high precipitation in the area at an altitude between 2500~4000m. It  
395 results in two high precipitation regions during the monsoon season (Fig.6 i), which are reflected in the zones of high  
396 susceptibility to RTL. The precipitation pattern is different from the PGA distribution (Fig.6 j) for the Gorkha  
397 earthquake, with strong shaking area located in the North and North east of Kathmandu, with PGA values larger than  
398 0.44g.

399 The distribution of RTL and ETL susceptibility classes are also very different. As the ETL susceptibility map is based  
400 on a single event, the distribution of the susceptibility classes is controlled by the PGA for the 2015 Gorkha  
401 earthquake, and the patterns of the ETL susceptibility map differs from the RTL susceptibility map. This was  
402 confirmed by the cross validation (Fig. 9), which showed that the RTL susceptibility map has a modest capability of  
403 explaining the ETL pattern, but that the ETL susceptibility cannot properly predict the RTLs.

404 This means one should be careful with using susceptibility maps that were made for earthquake induced landslides, as  
405 prediction tools for rainfall induced landslides. Such maps are in fact of little practical implication, as the next  
406 earthquake may not be likely to occur in the same location and therefore produce a similar landslide pattern. The  
407 generation of ETL susceptibility maps should not be based on single earthquake scenario scenarios (Jibson, 2011), and  
408 ideally many earthquake scenarios should be used to model the overall ETL susceptibility. However, using PGA values  
409 based on probabilistic seismic hazard assessment might result in relatively poor statistical correlations with event-based  
410 inventories. Therefore, PGA maps and ETL inventories of specific earthquake scenarios are required to improve the  
411 statistical models. This requires more event-based ETL inventories, and efforts to generate worldwide digital databases  
412 should be encouraged (Tanyas et al., 2017a).

413 The relationship between ETL and RTL might also change over time. In the years after the occurrence of an  
414 earthquake, rainfall triggered landslide patterns tend to follow those of the coseismic landslides, as was  
415 demonstrated for example in the 2008 Wenchuan earthquake (Tang et al., 2016) and other areas (Marc et al., 2015).  
416 Rainfall-induced landslide activity is generally much higher in the first years after an earthquake, and generally  
417 decreases to pre-earthquake levels within a decade, due to depletion of co-seismic sediments, progressive coarsening  
418 of available sediments and revegetation (Fan et al., 2018b; Hovius et al., 2011; Marc et al., 2015). Landslide  
419 susceptibility map should also be updated after major earthquakes.

420 Both ETL susceptibility maps and RTL susceptibility maps show different patterns for large landslides, as compared to  
421 the small landslide or all landslides. In general the susceptibility maps, for both RTL and ETL, for all landslide sizes  
422 together show a large similarity with the ones for the small landslides only. This is due to the fact that the number of  
423 large landslides is quite limited as compared to the small landslides (See Table 1), and the samples used for generation  
424 the models for all landslides and only small landslides are almost the same. However, the resulting susceptibility  
425 patterns are quite different, and it is therefore questionable whether landslide susceptibility maps that are generated for  
426 all landslide size would be able to accurately predict the large landslides. More emphasis should be given to the  
427 evaluation of landslide size in susceptibility and subsequent hazard and risk assessment. This is relevant for analyzing  
428 the potential runout areas of landslides and for evaluation landslide damming susceptibility (Fan et al., 2014; 2018b).  
429 Therefore, size and trigger matter in landslide susceptibility assessment.

430

## 431 **9. Acknowledgements**

432 This research was supported by the National Natural Science Foundation of China (Grant No.41401007), the External  
433 Cooperation Program of BIC, Chinese Academy of Sciences (Grant No. 131551KYSB20130003). This study was also  
434 jointly supported by the Australian government funded Koshi Basin Programme at ICIMOD as well as ICIMOD's core  
435 funds contributed by the governments of Afghanistan, Australia, Austria, Bangladesh, Bhutan, China, India, Myanmar,

436 Nepal, Norway, Pakistan, Switzerland, and the United Kingdom.

437

438

439 **References**

440 Ayalew L and Yamagishi H (2005) The application of GIS-based logistic regression for landslide susceptibility  
441 mapping in the Kakuda-Yahiko Mountains, Central Japan. *Geomorphology* 65(1–2): 15-31.  
442 doi:10.1016/j.geomorph.2004.06.010

443 Bai S, Wang J, Lü GN, Zhou PG, Hou SS and Xu SN (2010) GIS-based logistic regression for landslide susceptibility  
444 mapping of the Zhongxian segment in the Three Gorges area, China. *Geomorphology* 115(1–2): 23-31.  
445 doi:10.1016/j.geomorph.2009.09.025

446 Burg JP, Guiraud M, Chen GM and Li GC (1984) Himalayan metamorphism and deformations in the North Himalayan  
447 Belt (southern Tibet, China). *Earth Planet Sci Lett* 69:391–400.

448 Chang KT, Chiang SH and Hsu ML (2007) Modeling typhoon- and earthquake-induced landslides in a mountainous  
449 watershed using logistic regression. *Geomorphology* 89(3-4): 335–347. doi:10.1016/j.geomorph.2006.12.011

450 **Clauset A, Shalizi CR and Newman ME (2009) Power-law distributions in empirical data. *SIAM Review* 51(4): 661–**  
451 **703. <https://doi.org/10.1137/070710111>**

452 Collins BD and Jibson RW (2015) Assessment of existing and potential landslide hazards resulting from the April 25,  
453 2015 Gorkha, Nepal earthquake sequence. U.S. Geological Survey OpenFile Report 2015-1142, Reston, VA

454 Dai FC and Lee CF (2001) Frequency-volume relation and prediction of rainfall-induced landslides. *Engineering*  
455 *Geology* 59(3-4): 253-266. doi:10.1016/S0013-7952(00)00077-6

456 Dahal RK and Hasegawa S (2008) Representative rainfall thresholds for landslides in the Nepal Himalaya.  
457 *Geomorphology* 100 (3-4): 429–443. doi:10.1016/j.geomorph.2008.01.014

458 Das I, Sahoo S, van Westen CJ, Stain A and Hack R (2000) Landslide susceptibility assessment using logistic  
459 regression and its comparison with a rock mass classification system, along a road section in the northern  
460 Himalayas (India). *Geomorphology* 114(4): 627-637, doi:10.1016/j.geomorph.2009.09.023

461 Dhital MR (2015) *Geology of the Nepal Himalaya, Regional Perspective of the Classic Collided Orogen*, Springer,  
462 Switzerland. doi:10.1007/978-3-319-02496-7

463 Dilley M, Chen RS, Deichmann U, Lerner-Lam AL and Arnold M (2005) *Natural disaster hotspots: a global risk*  
464 *analysis*, The World Bank Hazard Management Unit, Washington

465 **Fawcett T (2006); An introduction to ROC analysis. *Pattern Recognition Letters* 27:861–874**

466 **Fan X Y, Qiao J P, Meng H, et al. (2012) Volumes and movement distances of earthquake and rainfall-induced**

467 catastrophic landslides. *Rock & Soil Mechanics*, 33(10):3051-3058.

468 Fan X, Rossiter DG, van Westen CJ, Xu Q and Görüm T (2014) Empirical prediction of coseismic landslide dam  
469 formation: coseismic landslide dam formation. *Earth Surf. Process. Landf.* 39: 1913–1926

470 Fan X, Domènech G, Scaringi G, Huang R, Xu Q, Hales T C, Dai L, Yang Q and Francis O (2018a) Spatio-temporal  
471 evolution of mass wasting after the 2008 Mw 7.9 Wenchuan Earthquake revealed by a detailed multi-temporal  
472 inventory. *Landslides*. doi: 10.1007/s10346-018-1054-5, 2018

473 Fan X, Juang CH, Wasowski J, Huang R, Xu Q, Scaringi G, van Westen CJ and Havenith H-B (2018b). What we have  
474 learned from the 2008 Wenchuan Earthquake and its aftermath: A decade of research and challenges. *Eng. Geol.*  
475 241: 25–32

476 Frattini P and Crosta GB (2013) The role of material properties and landscape morphology on landslide size  
477 distributions. *Earth and Planetary Science Letters* 361: 310-319. doi: 10.1016/j.epsl.2012.10.029

478 Froude MJ and Petley DN (2018) Global fatal landslide occurrence from 2004 to 2016. *Natural Hazards and Earth  
479 System Sciences*, 18: 2161-2181

480 Gansser A (1964) *Geology of the Himalayas*, Interscience, New York

481 Gurung HB and Khanal NR (1987) *Landscape processes in the Chure range, Nepal* National Committee for Man and  
482 the Biosphere, Kathmandu

483 Guzzetti F, Ardizzone F, Cardinali M, Rossi M and Valigi D (2008) Landslide volumes and landslide mobilization rates  
484 in Umbria, central Italy. *Earth and Planetary Science Letters* 279(3-4): 222-229. doi:10.1016/j.epsl.2009.01.005

485 Guzzetti F, Mondini AC, Cardinali M, Fiorucci F, Santangelo M, and Chang K -T (2012) Landslide inventory maps:  
486 New tools for an old problem. *Earth-Science Reviews*, 112(1), 42-66

487 Haque U, Blum P, da Silva PF, Andersen P, Pilz J, Chalov SR, Malet J-P, Auflič MJ, Andres N, Royiadji E, Lamas PC,  
488 Zhang W and Peshevski I (2016) Fatal landslides in Europe. *Landslides* 13(6): 1545–1554. doi:10.1007/s10346-  
489 016-0689-3

490 Highland LM and Bobrowsky P (2008) *The landslide handbook-A guide to understanding landslides*: Reston, Virginia,  
491 U.S. Geological Survey Circular 1325, 129 p.

492 Hodges KV, Parrish RR and Searle MP (1996) Tectonic evolution of the central Annapurna Range, Nepalese Himalaya.  
493 *Tectonics*, 15:1264-1291

494 Hovius N, Stark CP and Allen PA (1997) Sediment flux from a mountain belt derived by landslide mapping. *Geology*  
495 25(3): 231–234. [https://doi.org/10.1130/0091-7613\(1997\)025%3C0231:SFFAMB%3E2.3](https://doi.org/10.1130/0091-7613(1997)025%3C0231:SFFAMB%3E2.3).

496 Hovius N, Stark CP, Hao-Tsu C and Jiun-Chuan L (2000) Supply and removal of sediment in a landslide-dominated  
497 mountain belt: Central Range, Taiwan. *The Journal of Geology* 108(1): 73–89. <https://doi.org/10.1086/314387>.

498 Hovius N, Meunier P and Ching-weei L (2011) Prolonged seismically induced erosion and the mass balance of a large

499 earthquake. *Earth Planet. Sci. Lett.* 304: 347–355

500 Hussin HY, Zumpano V, Reichenbach P, Sterlacchini S, Micu M, van Westen CJ and Balteanu D (2016) Different  
501 landslide sampling strategies in a grid - based bi - variate statistical susceptibility model. *Geomorphology* 253:  
502 508-523

503 Jibson RW (2011) Methods for assessing the stability of slopes during earthquakes-A retrospective. *Eng. Geol.* 122:  
504 43–50

505 Kargel J, Leonard G, Shugar D. et al. (2016) Geomorphic and geologic controls of geohazards induced by Nepal's  
506 2015 Gorkha earthquake. *Science* 351(6269), aac8353. doi:10.1126/science.aac8353

507 Keefer DK (2002) Investigating landslides caused by earthquakes—a historical review. *Surv. Geophys.* 23:473-510

508 Kirschbaum D, Stanley T, and Zhou Y (2015) Spatial and temporal analysis of a global landslide catalog.  
509 *Geomorphology* 249:4-15

510 Klar A, Aharonov E, Kalderon-Asael B and Katz O (2011) Analytical and observational relations between landslide  
511 volume and surface area. *Journal of Geophysical Research* 116(F2): 1-10. doi:10.1029/2009JF00160 4

512 Korup O, Clague JJ, Hermanns RL, Hewitt K, Strom AL and Weidinger JT (2007) . Giant landslides topography and  
513 erosion. *Earth Planet. Sci. Lett.* 261, 578 - 589.

514 Larsen IJ and Montgomery DR (2012) Landslide erosion coupled to tectonics and river incision. *Nature Geoscience*  
515 5(7), 468–473. doi:10.1038/ngeo1479

516 Larsen IJ, Montgomery DR, Korup O (2011) Landslide erosion controlled by hillslope material. *Nature Geoscience*  
517 3(4), 247-251. doi:10.1038/ngeo776

518 Li G, West A J, Densmore A L, Jin Z, Parker R N, and Hilton R G (2014), Seismic mountain building: Landslides  
519 associated with the 2008 Wenchuan earthquake in the context of a generalized model for earthquake volume  
520 balance, *Geochem. Geophys. Geosyst.*, 15, 833–844, doi: 10.1002/2013GC005067.

521 Lin CW, Liu SH, Lee SY, Liu CC (2006) Impacts of the Chi-Chi earthquake on subsequent rainfall-induced landslides  
522 in central Taiwan. *Engineering Geology* 86(2-3): 87–101. doi:10.1016/j.enggeo.2006.02.010

523 Lin GW, Chen H, Hovius N, Horng MJ, Dadson S, Meunier P and Lines M (2008) Effects of earthquake and cyclone  
524 sequencing on landsliding and fluvial sediment transfer in a mountain catchment, *Earth Surf. Proc. Land.* 33:  
525 1354-1373

526 Liucci L, Melelli L, Suteanu C, Ponziani F (2017) The role of topography in the scaling distribution of landslide areas:  
527 A cellular automata modeling approach. *Geomorphology* 290: 236-249. doi:  
528 <https://doi.org/10.1016/j.geomorph.2017.04.017>

529 Pellicani R and Spilotro G (2015) Evaluating the quality of landslide inventory maps: comparison between archive and  
530 surveyed inventories for the Daunia region (Apulia, Southern Italy). *Bulletin of Engineering Geology and the*

531 **Environment 74(2): 357-367**

532 Peng L, Xu S, Peng J (2014). Research on development characteristics and size of landslide in the Three Gorges area.  
533 *Geoscience* 28(5): 1077-1086

534 Petley D (2012) Global patterns of loss of life from landslides. *Geology* 40: 927–930. doi:10.1130/G33217.1

535 Malamud BD, Turcotte DL, Guzzetti F and Reichenbach P (2004) Landslide inventories and their statistical properties.  
536 *Earth Surf. Process. Landform* 29:687-711. doi:10.1002/esp.1064

537 **Marc O, Hovius N, Meunier P, Uchida T and Hayashi S (2015). Transient changes of landslide rates after earthquakes.**  
538 ***Geology* 43, 883–886**

539 **Marc O and Hovius N (2015). Amalgamation in landslide maps: effects and automatic detection. *Nat. Hazards Earth***  
540 ***Syst. Sci.* 15:723–733**

541 **Marc O, Hovius N, Meunier P, et al. (2015) Transient changes of landslide rates after earthquakes. *Geology* 43(10):**  
542 **883-886**

543 Martha TR, Reddy PS, Bhatt CM, Govindha Raj KB, Nalini J, Padmanabha A, Narender B, Kumar KV,  
544 Muralikrishnan S, Rao GS, Diwakar PG and Dadhwal VK(2017a) Debris volume estimation and monitoring of  
545 Phuktal river landslide-dammed lake in the Zaskar Himalayas, India using Cartosat-2 images. *Landslides*  
546 14(1): 373-383. doi: 10.1007/s10346-016-0749-8

547 Martha TR, Roy P, Mazumdar R, Govindharaj KB and Kumar KV(2017b) Spatial characteristics of landslides  
548 triggered by the 2015 Mw 7.8 (Gorkha) and Mw 7.3 (Dolakha) earthquakes in Nepal. *Landslides* 14(2): 697–  
549 704. doi:10.1007/s10346-016-0763-x

550 **Meunier P, Hovius N and Haines JA (2008) Topographic site effects and the location of earthquake induced landslides.**  
551 ***Earth and Planetary Science Letters* 275(3-4): 221-232. doi:10.1016/j.epsl.2008.07.020**

552 Nandi A and Shakoor A (2010) A GIS-based landslide susceptibility evaluation using bivariate and multivariate  
553 statistical analyses. *Engineering Geology* 110(1–2): 11-20. doi:10.1016/j.enggeo.2009.10.001

554 **Razavizadeh S, Solaimani K, Massironi M and Kaviani A (2017) Mapping landslide susceptibility with frequency ratio,**  
555 **statistical index, and weights of evidence models: a case study in northern Iran. *Environmental Earth Sciences***  
556 **76(14), 499**

557 **Reichenbach P, Rossi M, Malamud BD, Mihir M and Guzzetti F (2018) A review of statistically-based landslide**  
558 **susceptibility models. *Earth-Science Reviews* 180: 60-91**

559 Roback K, Clark MK, West AJ, Zekkos D, Li G, Gallen SF, Champlain D, and Godt JW (2017) Map data of  
560 landslides triggered by the 25 April 2015 Mw 7.8 Gorkha, Nepal earthquake: U.S. Geological Survey data  
561 release, <https://doi.org/10.5066/F7DZ06F9>.

562 **Saba SB, van der Meijde M and van der Werff H. (2010) Spatio-temporal landslide detection for the 2005 Kashmir**

563 earthquake region. *Geomorphology* 124: 17-25

564 SafeLand (2015) Guidelines for landslide susceptibility, hazard and risk assessment and zoning,  
565 <https://www.ngi.no/eng/Projects/SafeLand>

566 Stark CP and Hovius N (2001) The characterization of landslide size distributions. *Geophysical Research Letters* 28:  
567 1091-1094

568 Tang C, Zhu J and Qi X (2010) Landslide hazard assessment of the 2008 Wenchuan earthquake: a case study in  
569 Beichuan area. *Canadian Geotechnical Journal* 48(1): 128-145. doi:10.1139/T10-059

570 Tang C, van Westen CJ, Tanyas H and Jetten VG (2016) Analysing post-earthquake landslide activity using multi-  
571 temporal landslide inventories near the epicentral area of the 2008 Wenchuan earthquake. *Nat. Hazards Earth*  
572 *Syst. Sci.* 16: 2641-2655. doi:10.5194/nhess-16-2641-2016

573 Tanyas H, van Westen, CJ, Allstadt KE, Jesse MA, Gorum T, Jibson RW, Godt JW, Sato HP, Schmidt RG, Marc O and  
574 Hovius N (2017a) Presentation and Analysis of a World-Wide Database of Earthquake-Induced Landslide  
575 Inventories. *Journal of Geophysical Research: Earth Surface* 122: 1991-2015

576 Tanyas H, van Westen CJ and Allstadt KE (2017b) New method for estimation of landslide-event magnitude based on  
577 large dataset of earthquake-induced landslides. *Earth Surface Processes and Landforms (Accept)*

578 ten Brink US, Barkan R, Andrews BD and Chaytor JD (2009) Size distributions and failure initiation of submarine and  
579 subaerial landslides. *Earth and Planetary Science Letters* 287: 31-42. doi: 10.1016/j.epsl.2009.07.031

580 Tong L, Qi S, An G and Liu C (2013) Large scale geo-hazards investigation by remote sensing in Himalayan region,  
581 Science Press, Beijing (in Chinese)

582 Wald DJ, Quitoriano V, Heaton TH and Kanamori H (1999) Relationship between Peak Ground Acceleration, Peak  
583 Ground Velocity, and Modified Mercalli Intensity for Earthquakes in California. *Earthquake Spectra*.  
584 <http://earthquake.usgs.gov/shakemap/global/shake/about.html#references>

585 Wang L, Sawada K and Moriguchi S (2013) Landslide susceptibility analysis with logistic regression model based on  
586 FCM sampling strategy. *Computers & Geosciences* 57: 81-92. doi:10.1016/j.cageo.2013.04.006

587 Zhang J, Gurung DR, Liu RK, Murthy MSR and Su FH (2015) Abe Berek landslide and landslide susceptibility  
588 assessment in Badakhshan Province, Afghanistan. *Landslides* 12(3): 597-609. doi: 10.1007/s10346-015-0558-5

589 Zhang J, Liu R, Deng W, Khanal NR, Gurung DR, Murthy MSR and Wahid S (2016) Characteristics of landslide in  
590 Koshi River basin, central Himalaya. *Journal of Mountain Science* 13(10):1711-1722. doi :10.1007/s11629-016-  
591 4017-0

592